Chemical Science

EDGE ARTICLE

View Article Online
View Journal | View Issue

Check for updates

Cite this: *Chem. Sci.*, 2025, **16**, 16090

All publication charges for this article have been paid for by the Royal Society of Chemistry

# $CO_2$ activation by gaseous zirconium cations: competition between spin-changing and spin-conserving pathways

Marcel Meta, †[a] Yang Liu, †[b] Martin Wedele,[a] Shaun G. Ard,[c]
Tucker W. R. Lewis,[c] Milan Ončák,[d] Nicholas S. Shuman,[c] Albert A. Viggiano,[c]
Hua Guo *[b] and Jennifer Meyer *[a]

Multi-state reactivity is a well-established concept to explain the surprising reactivity of open-shell systems when a spin-conserving channel is energetically inaccessible. Under such circumstances, the reaction is facilitated by intersystem crossing between different spin manifolds. Advancing the molecular-level understanding of multi-state reactivity requires well-defined model systems, which can be experimentally and theoretically treated at the required level of detail. The oxygen atom transfer from $CO_2$ to a transition metal cation in the gas phase presents such a prototype. Here, we present a joint experimental and theoretical study on the reaction dynamics and kinetics of $Zr^+ + CO_2$. Experimental energy and angle-resolved differential cross sections reveal dominant indirect atomistic dynamics in accord with recent studies on similar reactions with tantalum and niobium cations. Interestingly, trajectory simulations on full-dimensional coupled potential energy surfaces of the lowest-lying quartet and doublet electronic states of the $Zr^+ + CO_2 \rightarrow ZrO^+ + CO$ system from machine-learned first-principles data reveal a competition between an exothermic intersystem crossing pathway to $^2ZrO^+$ and an endothermic spin-conserving channel to $^4ZrO^+$. The experimental product ion velocity distributions are consistent with a switch of the dominant reaction channel when it is energetically allowed. The integral cross sections and thermal rate coefficients at low collision energies reveal three regimes with regard to the energy dependence of the integral cross section. A shift in energy dependence from $E^{-0.5}$ at the lowest energies at sub-Langevin values to $E^{-1}$ at intermediate energies, and finally to a positive energy dependence when the spin-conserving channel opens. These behaviors are well-explained by non-adiabatic transition-state theory and are distinctive of a submerged crossing point. The present study highlights the importance of spins revealing a delicate balance of their individual contributions to the interaction potential and resulting reaction dynamics.

Received 9th May 2025
Accepted 30th July 2025

DOI: 10.1039/d5sc03360h

rsc.li/chemical-science

## 1 Introduction

At present, there is a growing interest in single atom catalysis (SAC),[1–5] aiming for resource efficiency, *i.e.*, to catalyze chemical reactions with a minimum use of expensive transition metal catalysts, such as platinum, palladium and rhodium. SAC also facilitates precise control over the catalytic mechanism and product selectivity, thereby paving the way for beneficial applications of less-precious elements.[5,6] For these unique single site catalysts, the catalytic properties depend sensitively on their surroundings. Indeed, its oxidation state and the oxide substrate influence the reactivity and selectivity of the SAC through moderating its electronic structure, charge distribution, and coordination. A property that has gained more attention only recently is the spin of the metal active center,[7,8] which has previously been only thought about in relation to magnetic properties. It is well-established in homogeneous catalysis that metal spin can exert an appreciable influence on reactivity.[9]

In order to gain in-depth understanding of these effects, model systems are useful to reduce the complexity by making the reaction conditions controllable. While not all aspects of the real-life SAC can be addressed by a single model system, well-chosen models can target individual aspects experimentally and theoretically. Increasing complexity in a step-wise fashion then allows one to trace changes and to deduce structure/reactivity relations.

---

[a] *RPTU Kaiserslautern-Landau, Fachbereich Chemie und Forschungszentrum OPTIMAS, Erwin-Schrödinger Str. 52, 67663 Kaiserslautern, Germany. E-mail: jennifer.meyer@chem.rptu.de*

[b] *Department of Chemistry and Chemical Biology, Center for Computational Chemistry, University of New Mexico, Albuquerque, New Mexico 87131, USA. E-mail: hguo@unm.edu*

[c] *Air Force Research Laboratory, Space Vehicles Directorate, Kirtland Air Force Base, New Mexico 87117, USA*

[d] *Universität Innsbruck, Institut für Ionenenphysik und Angewandte Physik, Technikerstr. 25, 6020 Innsbruck, Austria*

† These authors contributed equally to this work.

Ion-molecule reactions in the gas phase are an established model system for transition metal chemistry.[10–20] Non-adiabatic dynamics are prevalent in gas phase chemistry involving open-shell reactants.[21–24] The spin state of the metallic SAC can be a crucial factor in heterogeneous catalysis, which can be dissected using isolated systems in the gas phase.

A well-studied prototype is the reaction between atomic metal cations $M^+$ and $CO_2$.[11,25–55] The activation of the greenhouse gas is of intense current interest in $CO_2$ remediation.[56] The observed activation of $CO_2$ by an oxygen-atom transfer reaction (OAT) at room temperature can, for many metals, only be explained by multi-state reactivity.[11,24] The importance of the intersystem crossing (ISC) for the reaction kinetics and dynamics was recently confirmed by experimental differential cross sections from crossed beam 3D velocity map imaging and thermal rate coefficients from selected-ion flow tube measurements. The experiments provided benchmark data for surface hopping trajectory simulations on full-dimensional coupled potential energy surfaces (PESs) for the reaction of $Ta^+$ and $Nb^+$ with $CO_2$.[35,36,57,58] Experiments and theoretical calculations reveal that both reactions are primarily governed by an indirect mechanism involving a long-lived pre-reaction well and product energy is predominantly distributed among the internal modes. Specifically, trajectory simulations clearly identify ISC as the key factor responsible for the kinetic bottleneck.

Importantly, these recent simulations showed no significant contributions of the spin-conserving channel (SCC) for $Ta^+$ + $CO_2$ or for $Nb^+$ + $CO_2$ at experimental energies of 0.46 eV and 0.17 eV above threshold, respectively.[57,58] Tantalum and niobium are both group V elements. Tantalum, as a 5d element, has a large spin–orbit coupling constant (SOC) of 329 $cm^{-1}$ between the lowest-lying quintet and triplet states. Its homologue, niobium, is a 4d element, and its SOC (127 $cm^{-1}$) is also relatively large. Thus, it is not surprising that the ISC is dominant even though the SCC is energetically accessible. In other words, the ISC presents less of a bottleneck compared to the potential barrier along the adiabatic pathway. Experimentally, the reaction threshold of the SCC can be determined by analyzing the kinetic energy dependence of the cross sections, as demonstrated by Sievers and Armentrout in their study of the $Nb^+$, $Zr^+$, and $V^+$ + $CO_2$ reactions using guided ion beam mass spectrometry (GIB-MS).[29,30,42] However, these values may not accurately reflect the true endothermicity of the SCC due to the competition of ISC. Therefore, theoretical insights are particularly valuable for understanding systems where ISC competes with spin conservation.

Another option to experimentally modify the strength of the SOC besides the use of the lighter homologue is to study reactions with an earlier transition metal, in this case zirconium.[25,30] The SOC near the crossing region for the zirconium reaction (38 $cm^{-1}$) is about a third that of niobium despite their similar masses. The zirconium oxide bond strength is higher than that of niobium. Hence, the reaction with zirconium is more exothermic for the spin-forbidden channel with ISC and less endothermic for the SCC than $Nb^+$ + $CO_2$, while being comparable to $Ta^+$ + $CO_2$. With the same relative collision energies accessible in the crossed beam experiment, we can now target the competition between the two channels (see reactions (1) and (2)).

$$^4Zr^+ + {}^1CO_2 \rightarrow {}^2ZrO^+ + {}^1CO \quad \Delta E = -2.3\ \text{eV} \tag{1}$$

$$\rightarrow {}^4ZrO^+ + {}^1CO \quad \Delta E = 1.4\ \text{eV} \tag{2}$$

These thermicities are consistent with the experimental and theoretical results of Armentrout[30] and the coupled cluster methods utilizing up to single, double, triple and quadruple excitations and complete basis set limit approximation (CCSDTQ/CBS)[59] as well as multi-reference configuration interaction (MRCI)[60] data.

Similar to the prior $Nb^+$ and $Ta^+$ studies, in this work, we present energy and angle-resolved differential cross sections for the title reaction from three-dimensional (3D) crossed beam velocity map imaging experiments at three different collision energies. Experimental results are compared to those from trajectory surface hopping simulations on full-dimensional coupled PESs machine learned from first principles data. The reaction dynamics study is complemented by thermal rate coefficient measurements from selected ion flow tube (SIFT) measurements and previous measurements of the integral cross section[30] and the thermal rate coefficient.[43] Simulations show a strong competition between the spin-changing (ISC, reaction (1)) and spin-conserving (SCC, reaction (2)) channels as function of the relative collision energy, which is found to be consistent with the experimental results. The present study shows the impacts of subtle differences in the potential energy landscape and interstate coupling even at relatively high collision energies investigated here.

## 2 Results and discussion

### 2.1 Reaction pathway/potential energy surface

The reaction pathway with the stationary points for the reaction between $Zr^+$ and $CO_2$ is shown in Fig. 1 and is broadly similar to those reported previously.[30,61] The reaction pathway is based on newly constructed full-dimensional PESs machine learned from density functional theory (DFT) data at the ωB97XD/DZ level of theory. Extensive benchmarking has been performed for the $Zr^+$ + $CO_2$ system (see SI) as well as for the corresponding $Ta^+$ + $CO_2$[35,57] and $Nb^+$ + $CO_2$[36,58] systems using a similar approach. The zirconium ion $Zr^+$ has a low-lying first excited electronic state ($^2D$) 0.42 eV above the ground state ($^4F$) at the ωB97XD/DZ level, which agrees well with the experimental value of 0.45 eV.[62] The experimental values are derived from the spin–orbit averaged energies of the $^4F$ and $^2D$ states,[62,63] whereas spin–orbit coupling effects were not included in the DFT calculations.

The thermalized population of the $^4F$ ground state is constrained to primarily the ground and first-excited spin–orbit states at room temperature. Both the lowest quartet and lowest doublet PESs have been constructed and the respective minimum energy pathways are shown here (quartet: red, doublet: blue). Starting from the free reactants in their respective ground states, a pre-reaction complex (RC) is formed in which the $CO_2$ attaches linearly to the metal ion, with the

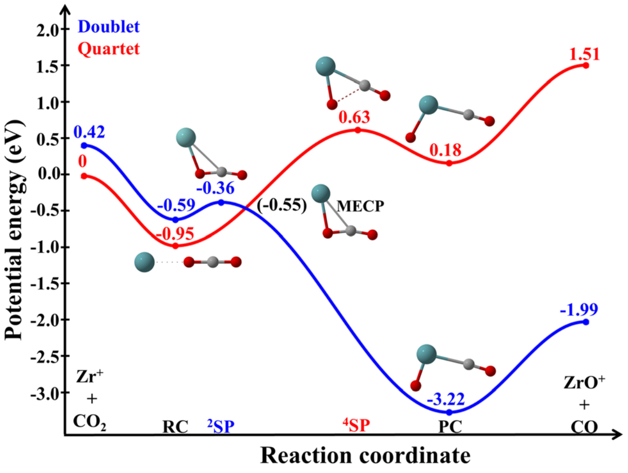

Fig. 1 Potential energy profile along the reaction coordinate for the $Zr^+ + CO_2 \rightarrow ZrO^+ + CO$ reaction on the quartet (red) and doublet (blue) state surfaces. All energies are in eV and relative to the quartet $Zr^+ + CO_2$ asymptote at the ωB97XD/DZ level. Zero-point energy correction is included. Please note that no ZPE is included for the MECP, which energy value is therefore given in brackets. Structures of the pre- and post-reaction minima, two saddle points, and the minimum energy crossing point (MECP) are given (blue = zirconium, grey = carbon, red = oxygen).

charge–quadrupole interaction the leading factor in the long-range potential.[64,65] The $[Zr^+CO_2]$ complex is stabilized by 0.95 eV relative to reactants, similar to that for $Ta^+$ and $Nb^+$.[35,36,57,58] The $CO_2$ tilts over, whereby an oxygen atom is transferred to the $Zr^+$. On the quartet PES, this occurs *via* a saddle point, $^4$SP, that is 0.63 eV above the reactant asymptote. The C═O bond is almost broken and $^4$SP resembles a $[OZrCO]^+$ product complex (PC) more than the $[ZrOCO]^+$ reactant complex. After abstraction of O, products are formed 1.51 eV above the reactant asymptote, *i.e.* the reaction is endothermic. If the reaction reaches the ground-state product channel ($^2ZrO^+ + CO_2$) *via* ISC, the reaction is exothermic by 1.99 eV. The submerged saddle point on the doublet PES ($^2$SP) is "earlier" along the reaction path than $^4$SP, closely resembling the entrance channel complex $^4$RC. After passing $^2$SP, the reaction proceeds through a deep post-reaction well before forming the free products $ZrO^+$ and CO. The reaction is rather efficient at room temperature, respectively at low collision energies, at about 60% of the Langevin collision rate (inclusion of the quadrupolar term marginally increases the calculated collision rate[66] by approximately 10% above the Langevin value).[25,30] An ISC from the quartet to the doublet state is required for this efficiency, given the endothermicity of the SCC. This behavior has been termed multi-state (or two-state) reactivity and is well established in gas-phase transition metal ion chemistry.[24,67] Similar to $Ta^+ + CO_2$ and $Nb^+ + CO_2$, the crossing point is located after the saddle point on the excited state PES. Thus, the reaction bypasses both saddle points along the minimum energy pathway (MEP).[57,58]

### 2.2 Integral cross section and reaction efficiency

Fig. 2a presents the calculated total integral cross sections (ICSs) for the $Zr^+ + CO_2 \rightarrow ZrO^+ + CO$ reaction as a function of relative collision energy ($E_{\mathrm{rel}}$) from fewest switches surface hopping (FSSH) calculations. In these simulations, the vibrational and rotational degrees of freedom of $CO_2$ were sampled at 300 K using a Boltzmann distribution. The experimental values measured by Sievers and Armentrout[30] are included in the same figure for comparison. Generally, our calculated ICSs agree well with the experimental measurements and exhibit a similar trend with the increment of $E_{\mathrm{rel}}$. For $E_{\mathrm{rel}}$ below 1.5 eV, ICSs decrease as $E_{\mathrm{rel}}$ increases, suggesting an indirect mechanism dominated by $^4$RC.

For collision energies larger than 1.5 eV, the ICS begins to rise until near 5.0 eV. The results can be attributed to the

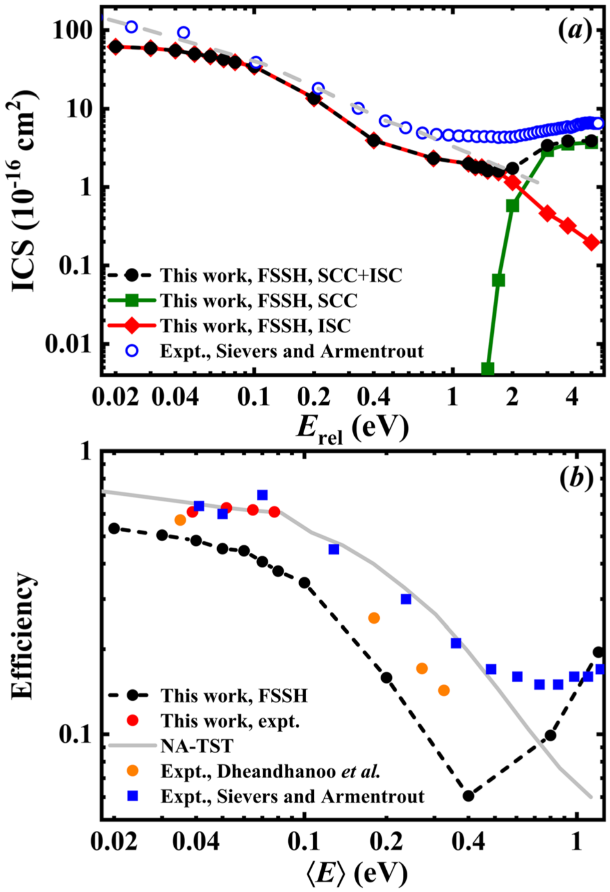

Fig. 2 (a) Comparison of the integral cross section (ICS) for the $Zr^+ + CO_2 \rightarrow ZrO^+ + CO$ reaction as a function of relative collision energy $E_{\mathrm{rel}}$ from fewest switches surface hopping (FSSH) calculations and experiment.[30,43] The gray dashed line shows the a model for exothermic formation of $ZrO^+$. This model, with an energy dependence of $E_{\mathrm{rel}}^{-1.0\pm0.1}$, is a fit to the experimental data in the low-energy region ($E_{\mathrm{rel}} < 0.75$ eV).[30] (b) Comparison of efficiencies as a function of thermal energy of $CO_2$, calculated using eqn (S6). The experimental reaction efficiencies are the ratio of the thermal rate coefficients to the capture limit.[66,68] Theoretical reaction efficiencies are determined by the ratio between the number of reactive trajectories and the number of captured trajectories.

formation of an excited state product $^4ZrO^+$. To gain insight into the reaction mechanism, the contributions of the ISC and SCC are also obtained and presented in the same figure. As shown in Fig. 2a, the SCC giving the quartet product opens at $E_{rel} = 1.5$ eV. Above the threshold, the ICS rises rapidly with increasing $E_{rel}$ before gradually slowing down at high collision energies. In contrast, the ICS leading to the doublet product decreases monotonically with increasing $E_{rel}$, which aligns with the model for the exothermic formation of $^2ZrO^+$ proposed by Sievers and Armentrout.[30] The results reveal a competition between the ISC and the SCC once the latter becomes energetically accessible ($E_{rel} \approx 1.5$ eV). This is in sharp contrast to the $Ta^+/Nb^+ + CO_2$ systems where the SCC is largely absent, at least until higher energies.[29,57,58] Compared to $Ta^+ + CO_2$, the key difference lies in the SOC values of the two reactions. The SOC for the $Zr^+ + CO_2$ reaction near the crossing seam is 38 $cm^{-1}$, significantly lower than the 330 $cm^{-1}$ value for the $Ta^+ + CO_2$ reaction. This is supported by the lifetimes of the RC complex (see Table 2). As shown in Fig. S1, at the same collision energy, RC in the $Zr^+ + CO_2$ system exhibits a significantly longer lifetime than those in the $Ta^+ + CO_2$ and $Nb^+ + CO_2$ reactions. This longer RC lifetime increases the likelihood of accessing the SCC. For $Nb^+ + CO_2$, not only the higher SOC value (127 $cm^{-1}$) but also the higher endothermicity of the SCC (2.17 eV), which is 0.50/0.67 eV higher than those for $Ta^+/Zr^+ + CO_2$, respectively, preventing the competition between the two channels at similar collision energies.

Reaction rate coefficients for $Zr^+ + CO_2$ were measured at 300, 400, 500, and 600 K using a SIFT apparatus (presented in Fig. 2b as efficiency relative to the Langevin capture value of $6.9 \times 10^{-10}$ $cm^3$ $s^{-1}$). These new data are complimentary to literature values of the reaction cross-section as a function of collision energy measured using a guided ion beam mass spectrometer (GIBMS) apparatus as well as rate coefficients measured as a function of translational energy using a drift tube apparatus.[30,43] The observed temperature dependence in the rate coefficient is close to zero at low energies, in agreement with the lowest energy GIBMS data as a function of translational energy only. The agreement of the beam data and temperature data at 600 K indicates that $CO_2$ vibrational excitation does not change the reactivity.[69]

At moderate energies, both the GIBMS and drift tube data show an $E^{-0.5}$ dependence in the rate coefficient corresponding to an $E^{-1}$ dependence in the cross section. Removing the energy dependence of the capture limit, the remaining $E^{-0.5}$ dependence matches that expected for an ISC under the assumptions of the Landau–Zener (LZ) treatment.[70] Because the relevant energy is that of nuclear motion near the crossing point, the relevant quantity is $E - E_{cp}$ (where $E_{cp}$ is the energy of the crossing point),[71,72] the flattening of the energy dependence at low energy could be due to the collision energy becoming small relative to $E_{cp}$.

The comparison of GIBMS and thermal data suggest that reactant internal energy is not effectively redistributed on the timescale of the entrance complex lifetime. Indeed, under the assumption that only reactant kinetic energy contributes, the observed change in the energy-dependence of the reaction efficiency from $E^0$ to $E^{-0.5}$ is quantitatively reproduced using non-adiabatic transition state theory (NA-TST).[73–75] Reaction efficiencies using the calculated structures without adjustable parameters (see SI for details) are shown in Fig. 2b and have excellent agreement with both experimental and trajectory results. The calculated Landau–Zener probability for adiabatic behavior is small, but this is offset by a frequency for sampling the crossing region that is large relative to that for back-dissociation. This is in contrast to the analogous $Nb^+ + CO_2$ and $Ta^+ + CO_2$ reactions, where the calculated Landau–Zener probability for adiabatic behavior is close to unity and the sub-collisional behavior is more likely due to inefficient sampling of the crossing region.

While the exceptional quantitative agreement between this simple model and the experiment/trajectory results shown in Fig. 2 must be somewhat fortuitous when considering the uncertainties in the calculated inputs and the assumptions inherent in the NA-TST approach, the reproduction of the sharp change in energy dependence allows a clear physical interpretation of the data. The reaction occurs in three distinct energetic regions. At the lowest energies (below about 0.1 eV) the reactivity is ISC-controlled and close to energy-independent. The ISC probability is dominated by the minimum energy dictated by the depth of the submerged crossing seam. The small energy dependence is expected to hold to lower temperatures and interestingly to remain sub-collisional even when approaching "zero" energy. This behavior is distinct for ISC at an energetically submerged crossing seam compared to that for an ISC with an activation barrier. At moderate energies (between about 0.1 and 1 eV), the efficiency falls more steeply with increasing energy ($E^{-0.5}$). Here, the collision energy becomes competitive with the energy of the submerged crossing seam (about −0.5 eV). The reaction is still ISC-controlled, but the Landau–Zener probability for adiabatic behavior is not constant as a function of energy. The third regime occurs at higher energies where the efficiency climbs rapidly as a new product channel opens. Although a number of excited doublet pathways are accessible at these energies, the dominant new pathway is most likely the spin-conserving quartet channel, evidenced by agreement with the trajectory calculations, which do not include the excited doublet pathways, and the likelihood that the kinetic preference is due to removing the ISC bottleneck.

It is worth noting that the experimental ICS and the associated modeling of the cross sections by Sievers and Armentrout indicate that the SCC opens at $E_{rel} \approx 0.62$ eV,[30] which is 0.88 eV lower than the threshold observed in our trajectory calculations. The FSSH calculations suggest an increase in the reaction efficiency as $E_{rel}$ nears 1 eV that is distinct from the opening of the SCC. The Sievers and Armentrout analysis attributed the rise in this region to the SCC, lowering the derived threshold, and this may account for the discrepancy. In any case, the experimental $^2ZrO^+/^4ZrO^+$ gap measured by Sievers and Armentrout[30] is $2.93 \pm 0.14$ eV, whereas our ωB97XD/DZ-level calculations yield a value of approximately 3.49 eV. This DFT result is consistent with the CCSD(T)/TZ//CCSD/DZ calculation (3.60 eV) performed in this study and the previously reported MRCI + Q calculation with the quadruple-ζ quality correlation consistent basis sets (3.66 eV).[60]

### 2.3 Energy and angle-resolved differential cross sections

The experimental differential energy and angular cross sections were recorded at three different relative collision energies $E_{\mathrm{rel}}$: 1.7, 2.2, and 3.3 eV (Fig. 3a–c). Product ion velocity distributions for $ZrO^+$ are shown in the center-of-mass frame and are normalized such that the bin with the highest number of entries is set to one. The dashed lines superimposed onto the distributions illustrate the kinematic cut-offs for the two considered electronic states of $ZrO^+$, doublet as the ground state (gray) and the first electronically excited state $^4ZrO^+$ (green). The kinematic cut-off gives the maximum possible velocity of $ZrO^+$ considering energy and momentum conservation. For all three relative collision energies, isotropic scattering around the center-of-mass is observed as the dominant scattering signature. This is a clear sign of indirect dynamics. A long-lived reaction intermediate is formed, which survives several rotational periods and subsequently scatters the product ions statistically in all spatial directions.[76,77] The full isotropy of the scattering angular distribution hints at efficient redistribution of angular momentum of the collision into rotational angular momentum of the molecular products.[76,78,79] With increasing relative collision energy, some trend towards scattering into the forward hemisphere, *i.e.*, a scattering angle $\theta$ below 90°, can be observed. This is more obvious in the integrated angular distributions shown in Fig. 3j–l (black solid line). This indicates a large momentum transfer related to a direct rebound mechanism, suggesting that the zirconium oxide turns around relative to the initial direction of the zirconium ion, a behavior consistent with low impact parameter collisions. Such a head-on approach geometry fits with the structure of the pre-reaction complex discussed before (see Fig. 1). The dynamics manifested here show the same trends as that observed previously for the reaction of $Ta^+$ and $Nb^+$ with $CO_2$.[35,36]

The distributions of the total product kinetic energy, *i.e.*, all energy partitioned into the movement of $ZrO^+$ and CO, are shown in the last row of Fig. 3m–o (black solid line). Events outside the area defined by the pie-cut shown in (a–c) are omitted from the analysis due to incomplete background subtraction (see Fig. S8 for comparison of the cut to the full distribution). The vertical dashed lines indicate the kinematic cut-offs with the shaded area around the cut-offs as the 1$\sigma$-error

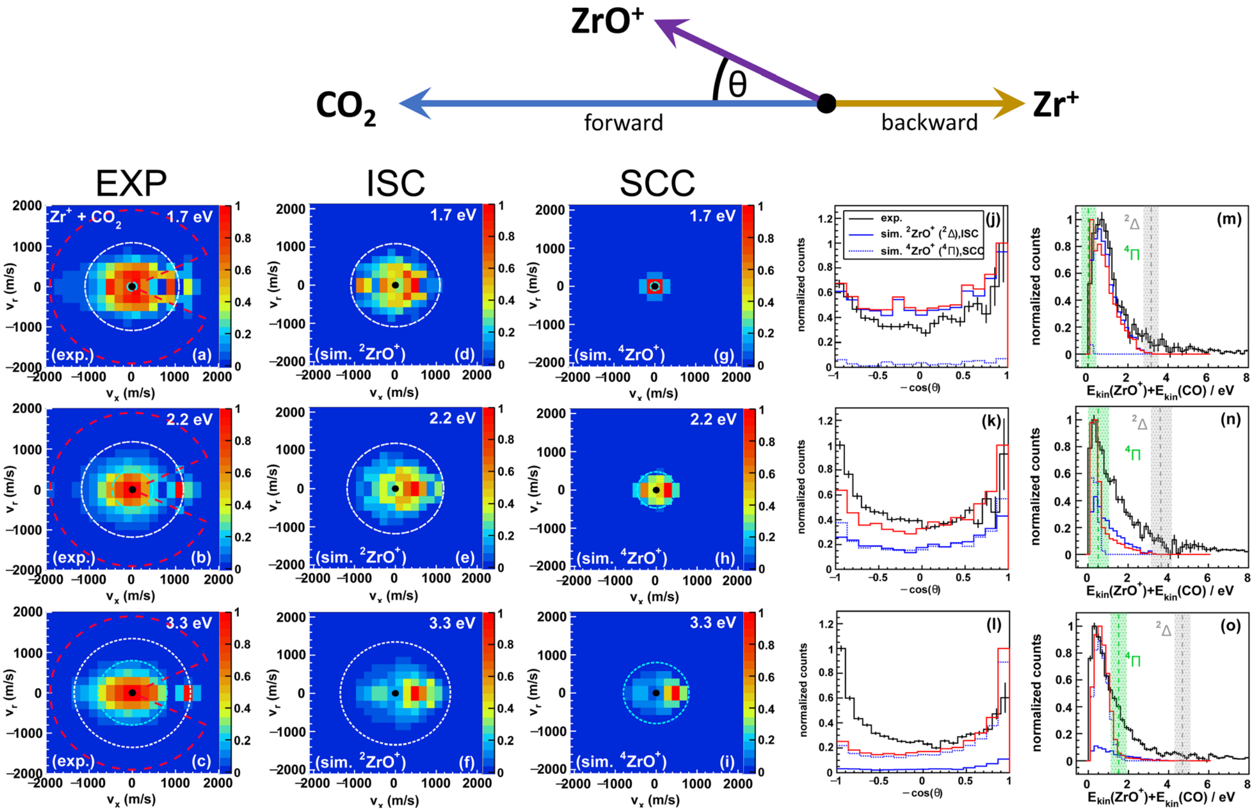

Fig. 3 Velocity distributions of $ZrO^+$ product ions at $E_{\mathrm{rel}} = 1.7$, 2.2, and 3.3 eV. In the first column (a–c) the experimental product ion velocity distributions are shown. Panels (d–f) show the velocity distributions for the spin-changing channel (ISC) and (g–i) for the spin-conserving channel (SCC) from FSSH simulation. The two superimposed circles (dashed lines) represent the kinematic cut-offs for $ZrO^+$ formation in the doublet $^2Zr^+$ (gray) and quartet $^4ZrO^+$ (green) state. (j–l) Give the integrated angular distributions and (m–o) integrated total product kinetic energy distributions. The experimental distributions (black) are directly compared to simulations (blue for the particular states and red for the weighted sum according to Table 2 ($^2ZrO^+$ = solid line, $^4ZrO^+$ = dashed line)). The dashed bars in (m–o) illustrate the respective kinematic cut-offs and the shaded area the 1$\sigma$-error of the experimental distribution.[80] For (m–o), experimental distributions are restricted to $\theta < 143°$ to exclude events from incomplete background subtraction. The evaluated scattering range is indicated by the pink pie cut in (a–c) and by the pink shaded area (j–l). All histograms are normalized. The top diagram illustrates the definition of the scattering angle by a simplified Newton diagram.

from Gaussian error propagation of the uncertainties of the reactant beams.[80] The integrated energy distributions highlight what can be seen in the 2D histogram of the velocity distributions in (a–c) in a more quantitative fashion: all three distributions are very similar to each other. Velocity distributions of $ZrO^+$ from the trajectory simulations are shown as a direct comparison to the experiment in Fig. 3 as well. In the second row (d–f), the results for the ISC channel ($^4Zr^+ + CO_2 \rightarrow {}^2ZrO^+ + CO$) are plotted and in the third row (g–i) the results for the (SCC) ($^4Zr^+ + CO_2 \rightarrow {}^4ZrO^+ + CO$) are shown. The integrated angular distributions are plotted in (j–l) in direct comparison to the experiment ($ZrO^+$: red solid line, $^2ZrO^+$: solid blue line, $^4ZrO^+$: dashed blue line). The distributions of different product states are scaled according to the branching ratio found in the simulations (Table 2). The simulations also reveal indirect scattering dominates, as seen in the experiment for both possible product states. The agreement between theory and experiment is very good at the two lower experimental collision energies. Deviations between experiment and theory appear at the highest investigated relative collision energy. The simulations find preferred scattering into the backward hemisphere, *i.e.*, in the initial direction of the ion beam. Direct forward scattering is typically associated with large reactive impact parameters and little momentum transfer. However, the experiment finds the opposite: large momentum transfer associated with small impact parameters. A similar discrepancy has been observed previously for tantalum and niobium.[57,58] This systematic deviation might be associated with the treatment of the spin–orbit coupling and/or the electronic state description in the entrance channel. A comparison of the product translational energy distributions shows very good agreement between theory and experiment (see Fig. 3m–o). The distributions from the simulations are generally narrower than the experiment, which is due presumably to the experimental energy spread of the reactant beams, not considered in the simulations. A comparison of the product ion kinetic energy $ZrO^+$ and the internal energy distributions are plotted in Fig. S4, and clearly shows that most of the additional energy from the collision is partitioned into internal degrees of freedom of either $ZrO^+$ or CO. While the experiment gives a mean excited fraction $f_{\text{int}}$ of about 0.5–0.6, theory is closer to $f_{\text{int}} = 0.8$ (Table 1). Interestingly, these values are similar for both reaction channels, the exothermic ISC crossing (reaction (1)) and the endothermic (SCC) (reaction (2)).

Table 1 Fraction of available energy $f_{\text{int}}$ partitioned into internal excitation using the mean of the internal energy distribution (Fig. S4). The total available energy given by $E_{\text{rel}}$ plus reaction energy from $^4Zr^+ + {}^1CO_2 \rightarrow ZrO^+ + {}^1CO$ for the two product channels[b]

| | Exp. | | Sim. | |
|---|---|---|---|---|
| $E_{\text{rel}}$/eV | $^2ZrO^+$ | $^4ZrO^+$ | $^2ZrO^+$ | $^4ZrO^+$ |
| 1.7 | 0.57 | — | 0.78 | —[a] |
| 2.2[b] | 0.54 | 1.11 (0.50) | 0.80 | 0.78 |
| 3.3 | — | 0.32 (0.58) | 0.70 | 0.75 |

[a] Fraction at threshold is not meaningful due to statistics. [b] The first number gives the internal fraction using all counts and the reaction energy assuming ISC. The number in parentheses is calculated assuming spin conservation and takes only events within the kinematic cut-off of the SCC channel into account.

# 3 Discussion

## 3.1 Product branching ratio

We often associate internal excitation with ro-vibrational excitation. Here, we also find a significant contribution of an excited electronic state of the $ZrO^+$ in the simulations. The analysis of the reactive trajectories allows the determination of a branching ratio for $ZrO^+$ formed in two different electronic states: ground doublet state $^2ZrO^+$ or the electronically excited quartet state $^4ZrO^+$. At the lowest collision energy, the SCC is barely energetically open and we expect no significant contribution. Contrary to the tantalum and niobium counterparts, the SCC significantly gains intensity with increasing collision energy to the point of becoming the major channel at the highest experimental collision energy of 3.3 eV (see Table 2). The histograms for angular and product kinetic energies in Fig. 3j–o show the individual contributions of both channels (blue lines). The experiment has no direct access to this ratio because most events are scattered into low velocities around the center-of-mass and thus within both relevant kinematic cut-offs. What we can say, however, is that experimental distributions are compatible with the theoretical branching ratio. At $E_{\text{rel}} = 3.3$ eV, most events can be found within the kinematic cut-off defined by the SCC channel. Interestingly, the SCC shows similar dynamical features to the ISC pathway with dominant indirect dynamics. The reaction encounters a bottleneck for both pathways which traps the system in a potential well along the reaction pathway. In case of the expected ISC channel, the bottleneck is the crossing point. This can be deduced from the hopping probability distributions. These show the number of "hops", *i.e.*, transitions needed to go from quartet to doublet on the way to product formation. In the ISC channel, the overwhelming number of reactive trajectories only "hops" once (see Fig. S5). In other words, once an ISC event occurs, product formation is irreversible. This is in-line with the greater than picosecond lifetime of the reactant complex at low collision energy (see $\tau_{\text{RC}}$, Table 2). In the collision complex, $^4$RC, energy is

Table 2 Branching ratio of doublet (ISC channel) to quartet (SCC channel) for product spin state of $ZrO^+$ from FSSH simulations and average lifetime of the $[Zr^+ + OCO]$ pre-reaction complex ($\tau_{\text{RC}}$) and of the exit channel complex $ZrO^+CO$ ($\tau_{\text{PC}}$) for the reactive trajectories. Additionally, $\tau_{\text{RC}}$ values are provided for trajectories in which reactants are trapped in the entrance complex but ultimately dissociate back to reactants

| | $^2ZrO^+$ (ISC) | | | $^4ZrO^+$ (SCC) | | | $^4Zr^+ + CO_2$ |
|---|---|---|---|---|---|---|---|
| $E_{\text{rel}}$/eV | % | $\tau_{\text{RC}}$/fs | $\tau_{\text{PC}}$/fs | % | $\tau_{\text{RC}}$/fs | $\tau_{\text{PC}}$/fs | $\tau_{\text{RC}}$/fs |
| 1.7 | 93 | 1360 | 470 | 7 | 1170 | 1650 | 415 |
| 2.2 | 45 | 1090 | 340 | 55 | 870 | 590 | 336 |
| 3.3 | 11 | 480 | 240 | 89 | 360 | 240 | 242 |

efficiently redistributed into rotational and vibrational degrees of freedom. Once the complex "hops", the rest of the energy freed in the reaction is mostly partitioned into product translation, leading to the observed near constant kinetic energy release. The SCC has no energetic transition state and the endothermicity is the kinetic constraint. Here, no additional reaction energy can be redistributed as for the ISC channel. We have two competing parallel reaction pathways. That the thermodynamically less favored channel dominates once it is energetically accessible strongly suggests that its bottleneck is much less restrictive (tight) than the thermodynamically favored one. This is completely the opposite behavior to that seen in the corresponding reactions with $Ta^+$ and $Nb^+$, neither of which showed a sizable contribution from the SCC at energies comparably above threshold.[57,58] At higher collision energies, the SCC in the $Nb^+ + CO_2$ reaction likely does dominate, evidenced by an increasing cross-section observed using GIB-MS.[29]

Exemplary trajectories for the two pathways are shown in Fig. 4 for the same impact parameter. Fig. 4a shows a typical trajectory for the ISC at $E_{rel} = 1.7$ eV. The $CO_2$ attaches to the $Zr^+$ but loosely bounces around for quite some time before one of the oxygen atoms binds to zirconium. The $CO_2$ tilts over before the C═O bond is fully cleaved and CO released. Note that the fully co-linear geometry predicted by the stationary points is not as prominent in the trajectories as could be expected. A SCC trajectory is shown in Fig. 4b at $E_{rel} = 3.3$ eV. The initial pre-reaction geometry is similar to that in the ISC channel, but the saddle point is later along the reaction pathway with a cleaved C═O bond and an almost fully formed CO attached to zirconium at some point. In terms of the Polanyi rules, the crossing point is "early", while the quartet saddle point is "late" along the reaction pathway.

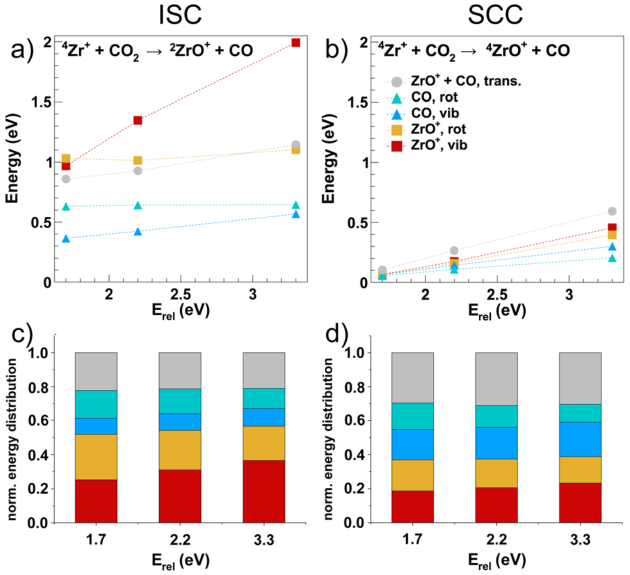

Fig. 5 Calculated average energy partitioning as a function of the collision energy for the spin-changing (ISC) (a and c) and the spin-conserving (SCC) (b and d) channels. Dashed lines are to guide the eye. Panels (a and b) give the absolute energy values for the amount of energy partitioned into translation (sum) and rotation and vibration for each product $ZrO^+$ and CO in eV. Panels (c and d) show the relative contributions to the total available energy of the different degrees of freedom in %. The color scheme is the same for all panels and symbols the same for panels (a and b): translation = grey, dots; $ZrO^+$, rot = orange, squares; $ZrO^+$, vib = red, squares; CO, rot = green, triangles; CO, vib = blue, triangles.

### 3.2 Ro-vibrational excitation

The trajectory simulations allow us to analyze how much energy is partitioned (1) into which product molecule and (2) into which degree(s) of freedom. Fig. 5 shows the mean amount of

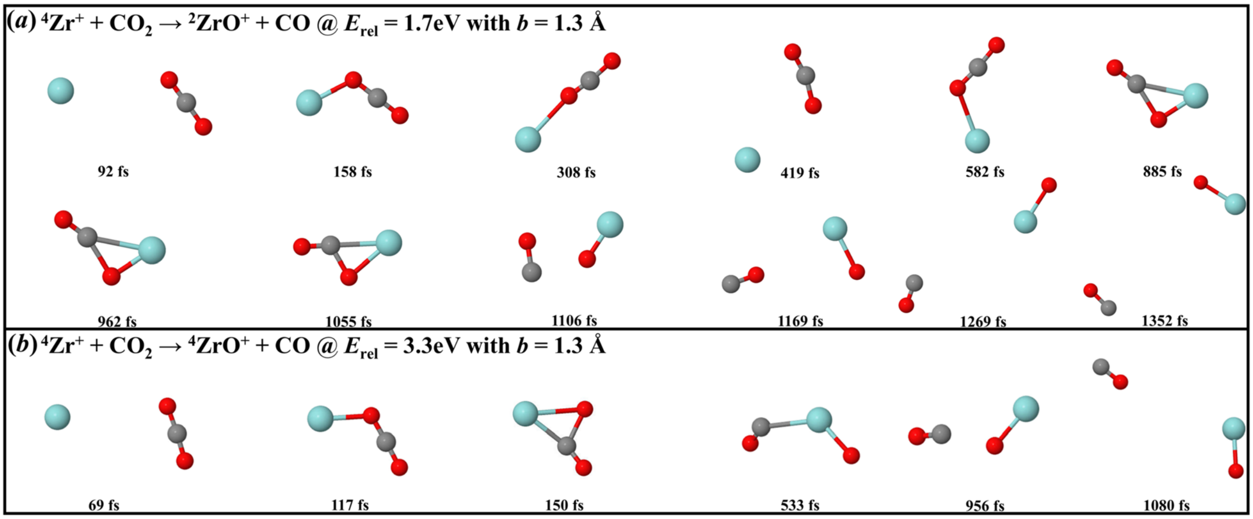

Fig. 4 Exemplary trajectories for the spin-changing channel (ISC) at $E_{rel} = 1.7$ eV (a) and spin-conserving channel (SCC) at $E_{rel} = 3.3$ eV (b) each for an impact parameter of $b = 1.3$ Å. Selection is such that only the dominant channel is shown. Full movies can be found in the SI (zirconium = blue, carbon = gray, oxygen = red).

energy partitioned into relative translation of $ZrO^+$ and CO and into rotations and vibration of each molecule following the ISC (a) and the SCC (b) in absolute values. The complete state distributions from which the mean values are calculated are shown in blue Fig. S6. In panel (a), it becomes obvious that CO in general receives less energy than $ZrO^+$ and that the partitioning into CO is comparable to that partitioned into product translation in both magnitude and trend. Additional collision energy is prominently partitioned into the $ZrO^+$ vibration with the rotational excitation also nearly independent of collision energy. For $ZrO^+$ + CO, energy partitioning is similar to $NbO^+$ + CO,[58] while for $TaO^+$ + CO most energy is partitioned into rotation of $TaO^+$.[57] The most striking difference compared to the two previously investigated systems $Ta^+/Nb^+ + CO_2$[35,36,57,58] is that here the additional collision energy is almost exclusively partitioned into a single mode, namely the $ZrO^+$ stretching mode. To better understand product energy disposal, we employed the Sudden Vector Projection (SVP) model,[81,82] which assumes that the energy distributed into a product mode is proportional to its projection onto the reaction coordinate at the transition state. The calculated SVP values for the $^2$SP are 0.224 and 0.066 for the vibrations of $ZrO^+$ and CO, respectively; 0.439 and 0.567 for the rotations of $ZrO^+$ and CO; and 0.537 for the translational mode. The SVP predictions align reasonably well with the energy distribution shown in Fig. 5a but overestimate the rotational excitation of CO. This discrepancy may arise because the crossing seam lies slightly on the product side of $^2$SP, as observed in the $Ta^+ + CO_2$ system.[57] The energy partitioning for the SCC is shown in Fig. 5b. It suggests an almost equal partitioning into all modes. Additional collision energy is distributed between all modes which can be seen in the same collision energy dependence. The relative contribution of all the different modes to the energy budget is shown in Fig. 5c and d for the two channels. By inspection, $ZrO^+$ (red-orange bars) gains more energy than CO (blue-greenish bars) in the ISC pathway upon increasing the collision energy, while in the SCC pathway the relative contributions of the different modes are not nearly as affected by increasing the collision energy. Even though the absolute amount of energy partitioned into translation is higher for the exothermic ISC channels, its relative contribution to the energy budget is lower than for the endothermic SCC (gray bars in Fig. 5c and d). Since the product energy disposal of the SCC is not governed by $^4$SP, the SVP values were not computed for this state.

### 3.3 Conclusions

Presented here is a joint experimental and theoretical study on the oxygen atom transfer reaction between $Zr^+$ and $CO_2$. The dynamics of the reaction were investigated by reactive scattering experiments using crossed beam 3D velocity map imaging and multi-state non-adiabatic dynamical calculations on full dimensional coupled potential energy surfaces (PESs) with doublet and quartet spin characters with spin–orbit couplings (SOCs) determined from multi-reference configuration interaction calculations. The thermal kinetics of the reaction were studied using a selected-ion flow tube along with comparison to the same calculations. The results are also compared to prior similar investigations of the $Ta^+$ and $Nb^+ + CO_2$ reactions[35,57,58] and to cross sections taken previously.[30]

We find, in general, good agreement between experiment and theory. The measured kinetics agree well with both literature values and the trajectory calculations, showing a distinct change in the collision-energy dependence, from $E^{-0.5}$ at energies below 0.1 eV to $E^{-1}$ at energies greater than 0.5 eV but below the onset of the spin conserving channel (SCC). Application of non-adiabatic transition state theory reproduces this change and suggests that the behavior is indicative of reactivity inhibited by a weakly coupled, submerged crossing seam. This contrasts with the $Ta^+/Nb^+$ reactions, which despite superficially very similar reaction coordinates and reaction efficiencies, are strongly coupled. Those are likely inhibited through limited access to the crossing region.

The calculations also well-reproduce the $ZrO^+$ product ion velocity and angular distributions. The differential cross sections (DCSs) reveal dominant indirect dynamics at all three investigated collision energies with more than half of the available energy partitioned into ro-vibrational excitation of the $ZrO^+$ and CO products. The collision energy is redistributed in the pre-reaction well with lifetimes on the order of a picosecond, which is also responsible for the largely isotropic angular distributions. The intersystem crossing (ISC) is the bottleneck along the reaction pathway as evidenced by the fact that a single "hop" from the quartet to the doublet occurs for product-forming trajectories. The resulting kinetic energy release is near constant and additional collision energy is partitioned almost exclusively into the $ZrO^+$ stretching vibration. At first glance, this looks similar to the previously studied $CO_2$ activation by transition metal cations $Ta^+$ and $Nb^+$. However, the simulations reveal a competition between the spin-changing (ISC) and the spin-conserving (SCC) channels. Our calculated integral cross sections (ICSs) over a wide collision energy range (0.02 to 5.0 eV), with the vibrational and rotational degrees of freedom of CO sampled at 300 K, show that the endothermic SCC channel becomes dominant as $E_{\mathrm{rel}}$ increases above 1.5 eV, *i.e.*, reaches the endothermicity of the channel. These insights help to explain the observed energy dependence of the ICS in this and previous experiments. Although the reactive scattering experiment cannot directly disentangle the contributions from both states given the experimental uncertainties, our data are consistent with the theoretically found branching ratio. The product ion velocity distributions for both channels show similarities but the energy partitioning is quite different. In the ISC pathway, additional collision energy is mostly partitioned into the $ZrO^+$ vibration, while in the endothermic SCC channel, additional collision energy is more uniformly distributed over all degrees of freedom. Once the endothermic channel is energetically accessible it dominates the product flux, suggesting that the quartet saddle point is not as tight as the crossing point, thus presenting less of a kinetic constraint. This was not seen before for $Ta^+ + CO_2$ and $Nb^+ + CO_2$ and underscores the sensitive balance between the SOC strength and the height of the energy barrier for the SCC. The good agreement between experiment and theory in the present study and in our other recent investigations[57,58,83] confirms the suitability of our approach. At the same time, it highlights the necessity for the study of these few atom model systems to build confidence in possible predictive methods for catalysis to be applied to larger and more complex systems. Such insights are expected to be vital for discovering new and more efficient single atom catalysts (SAC) catalysts for $CO_2$ activation.

## Author contributions

M. M. and M. W. carried out the crossed beam experiments; M. M., M. W. analyzed the crossed beam data; S. G. A. and T. W. R. L. carried out the SIFT experiments; S. G. A., T. W. R. L., A. A. V. and N. S. S. analyzed the SIFT data and performed the NA-TST modeling; M. O. performed and analyzed the quantum chemical calculations; Y. L. constructed the PESs and performed the trajectory calculations; Y. L. and H. G. analyzed the dynamics and kinetics; Y. L. performed and analyzed the SVP simulations; J. M., S. G. A. and N. S. S. supervised the experiment; M. M., Y. L., J. M. and H. G. prepared the manuscript; J. M. and H. G. coordinated the study.

## Conflicts of interest

There are no conflicts to declare.

## Data availability

The data supporting this article have been included as part of the SI. Additional data is available from the authors upon request.

Methods; Comparison of the RC lifetime in the $Zr^+/Nb^+/Ta^+ + CO_2$ reactions; Rate coefficients as a function of $\langle E \rangle$; Rate coefficients as a function of temperature; Comparison of experimental and theoretical internal and product ion kinetic energy distributions; (Average) Number of transitions required for hopping from quartet to doublet surface; Product energy distributions for $ZrO^+$ and CO; Potential energies along MEPs; Comparison of the cut to the full distribution; Absolute values of $E_{\mathrm{int}}$ and KER; Listing of the available molecular movies; Comparison of geometries in internal coordinates of the stationary points; ZPE-corrected energies and vibrational harmonic frequencies of the stationary points; Benchmarking of DFT functionals. See DOI: **https://doi.org/10.1039/d5sc03360h**.

## Acknowledgements

J. M. acknowledges support by the Deutsche Forschungsgemeinschaft DFG (project number 500279291). M. M. acknowledges support from the DFG through the SFB TRR88/3MET. Work at UNM was supported by Air Force Office of Scientific Research (FA9550-22-1-0350 to H. G.). Support for AFRL authors was provided by the Air Force Office of Scientific Research under AFOSR-25RVCOR006. T. R. W. L. was supported through the National Research Council Research Associateship Program. The computation was performed at CARC (Center for Advanced Research Computing) of the University of New Mexico and at the HPC infrastructure LEO of the University of Innsbruck. M. M., M. W. and J. M. thank Björn Bastian and Roland Wester for the use of the analysis program package for the crossed beam data. The authors thank Peter B. Armentrout for providing the numerical data of the integral cross sections. The views expressed are those of the authors and do not reflect the official guidance or position of the Department of the Air Force, the Department of Defense (DoD), or the U.S. government. The appearance of external hyperlinks does not constitute endorsement by the United States DoD of the linked websites, or the information, products, or services contained therein. The DoD does not exercise any editorial, security, or other control over the information you may find at these locations.

## References

1 R. Lang, X. Du, Y. Huang, X. Jiang, Q. Zhang, Y. Guo, K. Liu, B. Qiao, A. Wang and T. Zhang, *Chem. Rev.*, 2020, **120**, 11986–12043.

2 X.-F. Yang, A. Wang, B. Qiao, J. Li, J. Liu and T. Zhang, *Acc. Chem. Res.*, 2013, **46**, 1740–1748.

3 H. Schwarz, *Catal. Sci. Technol.*, 2017, **7**, 4302–4314.

4 A. K. Datye and H. Guo, *Nat. Commun.*, 2021, **12**, 895.

5 A. S. Dobrota and I. A. Pašti, *J. Phys. Chem. Lett.*, 2025, **16**, 77–86.

6 M. Melchionna and P. Fornasiero, *J. Am. Chem. Soc.*, 2025, **147**, 2275–2290.

7 F. Liu, T. Yang, J. Yang, E. Xu, A. Bajaj and H. J. Kulik, *Front. Chem.*, 2019, **7**, 219.

8 M. Li, W. Hu, B. Wang, Y. Li, W. Jian, J. Hao, L. Chen, C. Jia and X. Guo, *J. Am. Chem. Soc.*, 2025, **147**, 6193–6202.

9 P. W. N. M. van Leeuwen, *Homogeneous Catalysis: Understanding the Art*, Springer Netherlands, 2004.

10 M. M. Kappes and R. H. Staley, *J. Am. Chem. Soc.*, 1981, **103**, 1286–1287.

11 D. K. Bohme and H. Schwarz, *Angew. Chem., Int. Ed.*, 2005, **44**, 2336–2354.

12 Z. Luo, A. W. Castleman and S. N. Khanna, *Chem. Rev.*, 2016, **116**, 14456–14492.

13 J. Roithová and D. Schröder, *Chem. Rev.*, 2010, **110**, 1170–1211.

14 A. Fielicke, *Chem. Soc. Rev.*, 2023, **52**, 3778–3841.

15 S. G. Ard, A. A. Viggiano and N. S. Shuman, *J. Phys. Chem. A*, 2021, **125**, 3503–3527.

16 D. V. Fries, M. P. Klein, A. Steiner, M. H. Prosenc and G. Niedner-Schatteburg, *Phys. Chem. Chem. Phys.*, 2021, **23**, 11345–11354.

17 R. B. Metz, *Adv. Chem. Phys.*, 2008, **138**, 331–373.

18 K. R. Asmis and A. Fielicke, *Top. Catal.*, 2018, **61**, 1–2.

19 P. B. Armentrout, *Catal. Sci. Technol.*, 2014, **4**, 2741–2755.

20 G. Niedner-Schatteburg, in *Cooperative Effects in Clusters and Oligonuclear Complexes of Transition Metals in Isolation*, ed. S. Dehnen, Springer International Publishing, 2017, pp. 1–40.

21 D. Schroeder and H. Schwarz, *Angew. Chem., Int. Ed.*, 1990, **29**, 1433–1434.

22 J. N. Harvey, M. Diefenbach, D. Schröder and H. Schwarz, *Int. J. Mass Spectrom.*, 1999, **182–183**, 85–97.
23 J. N. Harvey, R. Poli and K. M. Smith, *Coord. Chem. Rev.*, 2003, **238–239**, 347–361.
24 D. Schroeder, S. Shaik and H. Schwarz, *Acc. Chem. Res.*, 2000, **33**, 139–145.
25 G. K. Koyanagi and D. K. Bohme, *J. Phys. Chem. A*, 2006, **110**, 1232–1241.
26 A. Iskra, A. S. Gentleman, E. M. Cunningham and S. R. Mackenzie, *Int. J. Mass Spectrom.*, 2019, **435**, 93–100.
27 H. Schwarz, *Coord. Chem. Rev.*, 2017, **334**, 112–123.
28 B. C. Sweeny, B. A. Long, A. A. Viggiano, S. G. Ard and N. S. Shuman, *J. Phys. Chem. A*, 2022, **126**, 859–869.
29 M. Sievers and P. Armentrout, *Int. J. Mass Spectrom.*, 1998, **179–180**, 103–115.
30 M. Sievers and P. Armentrout, *Int. J. Mass Spectrom.*, 1999, **185–187**, 117–129.
31 I. S. Parry, A. Kartouzian, S. M. Hamilton, O. P. Balaj, M. K. Beyer and S. R. Mackenzie, *Angew. Chem., Int. Ed.*, 2015, **54**, 1357–1360.
32 R. Wesendrup and H. Schwarz, *Angew. Chem., Int. Ed.*, 1995, **34**, 2033–2035.
33 N. Levin, J. T. Margraf, J. Lengyel, K. Reuter, M. Tschurl and U. Heiz, *Phys. Chem. Chem. Phys.*, 2022, **24**, 2623–2629.
34 L. G. Dodson, M. C. Thompson and J. M. Weber, *Annu. Rev. Phys. Chem.*, 2018, **69**, 231–252.
35 M. Meta, M. E. Huber, T. Michaelsen, A. Ayasli, M. Ončák, R. Wester and J. Meyer, *J. Phys. Chem. Lett.*, 2023, **14**, 5524–5530.
36 M. E. Huber, T. W. R. Lewis, M. Meta, S. G. Ard, Y. Liu, B. C. Sweeny, H. Guo, M. Ončák, N. S. Shuman and J. Meyer, *Phys. Chem. Chem. Phys.*, 2024, **26**, 8670–8680.
37 M. R. Sievers, Y. Chen and P. B. Armentrout, *J. Chem. Phys.*, 1996, **105**, 6322–6333.
38 M. R. Sievers and P. B. Armentrout, *J. Phys. Chem. A*, 1998, **102**, 10754–10762.
39 X.-G. Zhang and P. B. Armentrout, *J. Phys. Chem. A*, 2003, **107**, 8904–8914.
40 X.-G. Zhang and P. B. Armentrout, *J. Phys. Chem. A*, 2003, **107**, 8915–8922.
41 P. B. Armentrout, *Mass Spectrom. Rev.*, 2021, **41**, 606–626.
42 M. R. Sievers and P. B. Armentrout, *J. Chem. Phys.*, 1995, **102**, 754–762.
43 S. Dheandhanoo, B. K. Chatterjee and R. Johnsen, *J. Chem. Phys.*, 1985, **83**, 3327–3329.
44 M. Ghiassee, J. Kim and P. Armentrout, *J. Chem. Phys.*, 2019, **150**, 144309.
45 M. Ghiassee, B. Stevenson and P. Armentrout, *Phys. Chem. Chem. Phys.*, 2021, **23**, 2938–2952.
46 C. Owen, J. Kim and P. Armentrout, *J. Chem. Phys.*, 2021, **155**, 094303.
47 R. Cox, K. Harouaka, M. Citir and P. Armentrout, *Inorg. Chem.*, 2022, **61**, 8168–8181.
48 M. Ghiassee, E. Christensen, T. Fenn and P. Armentrout, *J. Phys. Chem. A*, 2023, **127**, 169–180.
49 A. Bubas, W.-J. Zhang and P. Armentrout, *J. Chem. Phys.*, 2023, **159**, 244305.
50 T. Fenn, B. Stevenson and P. Armentrout, *J. Chem. Phys.*, 2024, **128**, 7843–7855.
51 J. B. Griffin and P. B. Armentrout, *J. Chem. Phys.*, 1998, **108**, 8075–8083.
52 M. R. Sievers and P. B. Armentrout, *Inorg. Chem.*, 1999, **38**, 397–402.
53 M. Santos, J. Marcalo, A. P. de Matos, J. K. Gibson and R. G. Haire, *J. Phys. Chem. A*, 2002, **106**, 7190–7194.
54 M. Santos, J. Marcalo, J. P. Leal, A. P. de Matos, J. K. Gibson and R. G. Haire, *Int. J. Mass Spectrom.*, 2003, **228**, 457–465.
55 H. H. Cornehl, R. Wesendrup, M. Diefenbach and H. Schwarz, *Chem.–Eur. J.*, 1997, **3**, 1083–1090.
56 H. Arakawa, M. Aresta, J. N. Armor, M. A. Barteau, E. J. Beckman, A. T. Bell, J. E. Bercaw, C. Creutz, E. Dinjus, D. A. Dixon, K. Domen, D. L. DuBois, J. Eckert, E. Fujita, D. H. Gibson, W. A. Goddard, D. W. Goodman, J. Keller, G. J. Kubas, H. H. Kung, J. E. Lyons, L. E. Manzer, T. J. Marks, K. Morokuma, K. M. Nicholas, R. Periana, L. Que, J. Rostrup-Nielson, W. M. H. Sachtler, L. D. Schmidt, A. Sen, G. A. Somorjai, P. C. Stair, B. R. Stults and W. Tumas, *Chem. Rev.*, 2001, **101**, 953–996.
57 Y. Liu, M. Ončák, J. Meyer, S. G. Ard, N. S. Shuman, A. A. Viggiano and H. Guo, *J. Am. Chem. Soc.*, 2024, **146**, 14182–14193.
58 Y. Liu, M. Ončák, J. Meyer, S. G. Ard, N. S. Shuman, A. A. Viggiano and H. Guo, *J. Phys. Chem. A*, 2024, **128**, 6943.
59 C.-S. Lam, K.-C. Lau and C.-Y. Ng, *Mol. Phys.*, 2018, **116**, 2709–2718.
60 I. R. Ariyarathna and E. Miliordos, *J. Quant. Spectrosc. Radiat. Transfer*, 2020, **255**, 107265.
61 G.-L. Dai, C.-F. Wang, H. Chen, J.-Y. Wu, H. Yan and A.-G. Zhong, *Russ. J. Phys. Chem. A*, 2010, **84**, 2238–2246.
62 A. Kramida, Y. Ralchenko and J. Reader, *NIST Atomic Spectra Database*, NISTASD Team, **http://physics.nist.gov/asd/**.
63 J. Lawler, J. Schmidt and E. A. D. Hartog, *J. Quant. Spectrosc. Radiat. Transfer*, 2022, **289**, 108283.
64 M. Sodupe, V. Branchadell, M. Rosi and C. W. Bauschlicher, *J. Phys. Chem. A*, 1997, **101**, 7854–7859.
65 C. Heinemann, J. Schwarz and H. Schwarz, *Chem. Phys. Lett.*, 1995, **247**, 611–613.
66 P. K. Bhowmik and T. Su, *J. Chem. Phys.*, 1991, **94**, 6444–6445.
67 J. L. Elkind and P. B. Armentrout, *J. Phys. Chem.*, 1987, **91**, 2037–2045.
68 P. K. Bhowmik and T. Su, *J. Chem. Phys.*, 1986, **84**, 1432–1434.
69 A. A. Viggiano, *Phys. Chem. Chem. Phys.*, 2006, **8**, 2557–2571.
70 C. Wittig, *J. Phys. Chem. B*, 2005, **109**, 8428–8430.
71 S. G. Ard, O. Martinez, S. A. Brown, J. C. Sawyer, P. B. Armentrout, A. A. Viggiano and N. S. Shuman, *Phys. Chem. Chem. Phys.*, 2017, **19**, 8768–8777.
72 I. Kretzschmar, D. Schröder, H. Schwarz, C. Rue and P. B. Armentrout, *J. Phys. Chem. A*, 1998, **102**, 10060–10073.
73 J. C. Lorquet and B. Leyh-Nihant, *J. Phys. Chem.*, 1988, **92**, 4778–4783.
74 J. N. Harvey, *Phys. Chem. Chem. Phys.*, 2007, **9**, 331–343.

75 C. Rue, P. B. Armentrout, I. Kretzschmar, D. Schroder, J. N. Harvey and H. Schwarz, *J. Chem. Phys.*, 1999, **110**, 7858–7870.
76 D. R. Herschbach, *Angew. Chem., Int. Ed.*, 1987, **26**, 1221–1243.
77 R. N. Zare, *Angular Momentum*, John Wiley & Sons, 1988.
78 *Tutorials in Molecular Reaction Dynamics*, ed. M. Brouard and C. Vallance, RSC Publishing, 2012.
79 R. D. Levine, *Molecular Reaction Dynamics*, Cambridge University Press, 2009.
80 R. Wester, *Phys. Chem. Chem. Phys.*, 2014, **16**, 396–405.
81 B. Jiang and H. Guo, *J. Chem. Phys.*, 2013, **138**, 234104.
82 H. Guo and B. Jiang, *Acc. Chem. Res.*, 2014, **47**, 3679–3685.
83 Y. Liu, M. Ončák, T. W. R. Lewis, M. Meta, S. G. Ard, N. S. Shuman, J. Meyer, A. A. Viggiano and H. Guo, *Chem. Sci.*, 2025, **16**, 5007–5016.